Progress in Additive Manufacturing
https://doi.org/10.1007/s40964-022-00282-x

FULL RESEARCH ARTICLE

Experimental and numerical comparison of heat accumulation during laser powder bed fusion of 316L stainless steel

Mohsin Ali Chaudry[1] · **Gunther Mohr**[1,2] · **Kai Hilgenberg**[1]

Received: 25 October 2021 / Accepted: 27 February 2022

Abstract
Heat accumulation during laser powder bed fusion (LPBF) of metallic build parts can adversely affect their microstructure and mechanical properties. To study the heat accumulation during 316L steel based parts manufactured by LPBF, a finite element method (FEM) based numerical study is carried out. For the investigation, a computationally efficient FEM based model, where the whole layer is simultaneously exposed to a heat source, is used. The simulation results are compared with experimental results to validate the numerical model. While considering different influencing factors such as volumetric energy density (VED) and inter-layer time (ILT), the FEM model is shown to successfully simulate the process of heat accumulation during LPBF based manufacturing of a cuboidal shaped geometry. It is shown that ILT and VED have a significant effect on heat accumulation. The validated numerical model provides a good basis for the optimization of processing parameters and geometries for a future investigation of a reduction of heat accumulation effects. Furthermore, it can be used to quickly provide preheating boundary conditions for detailed investigations by different model approaches at a finer scale for future studies.

Keywords Laser powder bed fusion · Finite element method · Heat accumulation · Inter-layer time

1 Introduction

In recent years, considerable advances have been made in additive manufacturing (AM). Laser powder bed fusion (LPBF) is one of the AM based technologies, where metallic parts are produced by layer-wise melting and fusion of a metallic powder raw material. Currently, it has become one of the leading AM technologies to manufacture complex shaped and high precision engineering components with applications, among others, in medical, aerospace, and automotive industry. However, the effect of various influencing factors on the resultant product quality is still not fully understood.

✉ Mohsin Ali Chaudry
mohsin-ali.chaudry@bam.de

[1] 9.6 Additive Fertigung metallischer Komponenten, Bundesanstalt für Materialforschung und -prüfung, Unter den Eichen 87, 12205 Berlin, Germany

[2] Institute of Machine Tools and Factory Management, Technische Universität Berlin, Straße des 17, Juni, 10623 Berlin, Germany

The influence of laser processing parameters on the build quality is widely studied in the literature. For 316L steel based built part, Liverani et al. [1] studied the development of defects, change in mechanical properties and microstructure based on the laser processing parameters. Sames et al. [2] discussed the development of defects based on the processing parameters. Among the high number of influencing factors, the processing parameters laser power P in W, scanning velocity v in mm/s, and hatch distance h_d in mm are of utmost importance. An often used auxiliary factor combining the aforementioned parameters with the layer thickness t_l is the volumetric energy density (VED). It can be written as given below.

$$E = \frac{P}{v \cdot h_d \cdot t_l} \tag{1}$$

To reduce defect occurrence and to improve the build quality, optimizations of a combination of these parameters have been subject of many studies. For instance, a reduction of the scanning velocity leads to an increase of the VED and can result in a reduction of the well known lack of fusion problem. On the other hand, it can induce the occurrence of porosity due to unstable keyhole mode welding. In case

Published online: 21 March 2022

of a high scanning velocity, partial melting, narrow melt pools and high cooling rates can result. Similarly, for low laser power, which results in a low value of VED, lack of fusion can occur while with a higher value keyhole porosity can occur. Therefore, a parameter optimization has to be performed to determine the most suitable combination. However, as discussed by Bertoli et al. [3], caution should be exercised when using VED alone as a design criterion for the choice of appropriate process parameters as it does not capture the complex physics during LPBF. In the current work, the scanning velocity was varied to obtain different values of VED while standard values were used for other parameters, see Sect. 3.

In addition to these parameters, Mohr et al. [4] described the effect of geometry dependant processing parameters, including inter-layer time (ILT) and the build height, on the heat accumulation during manufacturing. Inter-layer time, which was described as the duration between the laser energy input of a volume element from one layer to the subsequent layer at the same x–y position, is also a critical parameter that can influence the presence of defects and the development of the microstructure of the built part. Denlinger et al. [5] studied the effect of ILT, referred there as dwell time, on the resulting distortion and residual stress during directed energy deposition based manufacturing of titanium and nickel based alloys. In their work, for nickel (Inconel 625) alloy, a decrease in distortion and residual stresses was observed for an increase in ILT while the opposite was observed for α/β titanium (Ti-6Al-4V). However, they concluded that an increase of the ILT results in a decrease in heat accumulation. Similarly, Costa et al. [6] studied the effect of the variation of ILT on AISI 420 steel based parts, which were manufactured via laser metal deposition (LMD). They concluded that an increase in ILT has a significant effect on the resultant microstructure and thermal history. As described by Mohr et al. [4, 7] and Williams et al. [8], a decrease in ILT leads to increased preheating temperatures as an initial condition for the subsequent new layer. The initial surface temperature can affect the solidification conditions and the geometry of the melt pool. In addition, due to heat accumulation with the decrease in ILT, tendency for the development of keyhole porosity increases. The accumulation of heat with the decrease in ILT can be ascribed to the decrease in the duration for energy dissipation into the already built part, substrate plate, and surrounding powder before the next energy input by absorption of laser radiation starts. This becomes more pronounced as the build height of the part increases. Mohr et al. [4] described this in detail for 316L based built parts.

For better understanding of such factors and an increase in awareness of their effects, numerical models can assist in carrying out a detailed analysis. The analysis can be carried out while considering different fields and scales. For instance, at the powder scale, Khairallah et al. [9] used a ray tracing algorithm together with thermal fluid dynamics to simulate the complex melt pool behaviour. Although such a fine scale model was able to reproduce several physical effects during the development of a melt pool, the computational cost associated with it was quite high. Denlinger et al. [10] used a transient thermal FEM model together with a volumetric heat source to predict the thermal field for IN718 during LPBF based manufacturing. In their model, the mesh size was a fraction of the melt pool and the scan path of the laser was traced. Similarly, Khan et al. [11] used an adaptive meshing for the simulation of LPBF of 316L with multiple tracks. Besides aforementioned conventional mesh-based methods, mesh-free methods have also been used for melt pool simulation. In the work of Furstenau et al. [12], a smoothed particle hydrodynamics (SPH) approach was used for the simulation of the 3D melt pool dynamics. The 3D SPH model included a novel approach for curvature calculation which was later used for a surface tension estimation. The computational efficiency was realized by a GPU accelerated implementation of the code. Russell et al. [13] adapted the SPH method to resolve thermal, mechanical and material fields for LPBF at a powder scale. Their 2D model was validated by a comparison with experimental results. Afrasiabi et al. [14] adapted the SPH approach in multi resolutions for the simulation of melt pool dynamics of LPBF single tracks. In their work, a computationally efficient approach was used for the resolution of thermal, mechanical, and material fields, where a dynamic particle refinement technique was applied.

The aforementioned models, both mesh based and meshless methods, are computationally feasible for simulation of small parts with only a few layers. In case of large parts with exposition of several layers, the computational cost associated with such models can be huge. Therefore, several simplifications are often made in the literature reduce the computational cost. For instance, Li et al. [15] and Denlinger et al. [16] used an equivalent heat source for layer by layer heat application. This allowed for the prediction of thermal history and distortion of large parts. A similar approach was also used in the current work to model the LPBF process.

In this study, a computationally efficient FEM model was developed that can predict the heat accumulation of 316L steel based built parts. For the analysis, the effect of different combinations of ILT and VED on the resultant heat accumulation was considered. The model also covered the experimentally observed penetration depth of the laser with the volumetric heat source. This will give a better understanding of the factors that are responsible for the heat accumulation and resultantly in defects in LPBF based build part. For the validation, the results from the FEM model were compared with the experimentally measured temperature data and limitations of the model were discussed. Such a comparative

experimental and numerical study for the heat accumulation of the entire LPBF part serves as an addition to the limited literature in this regard.

2 LPBF model description

LPBF, inherently, is a multiphysics process, where multiple fields such as thermal, displacement, and velocity field, among others, are involved. However, for the current investigation, the thermal field T is of primary interest and other fields, e.g., displacement are not considered. For the numerical modelling of LPBF, a pure transient thermal analysis is carried out. It is based on the following heat equation.

$$\rho c \frac{\partial T}{\partial t} = k\left(\frac{\partial^2 T}{\partial x^2} + \frac{\partial^2 T}{\partial y^2} + \frac{\partial^2 T}{\partial z^2}\right) + Q_v \tag{2}$$

Here, ρ represents the density, c the specific heat capacity, k the thermal conductivity, T the temperature, and Q_v represents the heat source. The material properties were assumed to be isotropic and temperature dependant. The variation of material properties with the temperature is described in Sect. 2.1. The heat input can be surface heat flux or volumetric heat source. In the current work, a volumetric heat source, described in Sect. 2.2, is used. For the solution of the partial differential equation, initial and boundary conditions are required. As an initial condition, the preheating temperature can be prescribed on the part of the body.

$$T(\boldsymbol{x}, 0) = T_0, \quad \text{on} \quad \Omega \cup \partial\Omega \tag{3}$$

Here, T_0 represents initial temperature, Ω represents the domain and $\partial\Omega$ represents the boundary of the domain. As a boundary condition, it is assumed that the heat loss from the free surface occurs due to convection, which can be calculated as given below.

$$q = h(T - T_\infty) \tag{4}$$

where T_∞ represents the ambient temperature and h represents the constant convection coefficient.

For the solution of the partial differential equation (PDE), it is first converted to weak form by multiplication with the test function, as given below.

$$\int_\Omega \delta T c \dot{T} \mathrm{d}\Omega - \int_\Omega \nabla \delta T \cdot (-k \nabla T) \mathrm{d}\Omega + \int_\Gamma \delta T \hat{q} \mathrm{d}\Gamma - \int_\Omega \delta T \boldsymbol{Q}_v \mathrm{d}\Omega = 0, \tag{5}$$

where δT represents the test function. This is later discretized into finite number of elements and solved using finite element method (FEM). In FEM, the primary unknown field variable T is represented with the linear isoparametric interpolation function as given below.

$$T(x, t) = \sum_j N_j T_j(t), \tag{6}$$

where N_j represents the interpolation function and $T_j(t)$ represents the unknown temperature at the node j of an element. For the solution, the transient thermal analysis solver of Ansys® Academic Research Mechanical, Release 2019R3 [17] is used.

2.1 Thermophysical parameters

The metallic powder (316L) undergoes different phase changes during laser scanning due to an increase in temperature from below the solidus temperature up to temperatures which exceed the liquidus temperature. During this transition, the thermophysical properties also change. Hence, these properties depend on the transient temperature, as reported by Mills [18]. In addition to the temperature dependency of the thermophysical properties, further deviation of the material properties has to be considered: for instance, due to point contact of powder particles, the thermal conductivity of powder k_{pwd} deviates from the conductivity of bulk solid. For the determination of k_{pwd}, following equation is used, as described by Sih et al. [19].

$$k_{\mathrm{pwd}} = k_{\mathrm{arg}}\left[\left(1 - \sqrt{1-\phi}\right)\left(1 + \phi\frac{k_{\mathrm{rad}}}{k_{\mathrm{arg}}}\right) + \sqrt{1-\phi}\left(\frac{2}{1 - k_{\mathrm{arg}}/k_{316\mathrm{L}}}\left(\frac{2}{1 - k_{\mathrm{arg}}/k_{316\mathrm{L}}}\right) + \ln\frac{k_{\mathrm{rad}}}{k_{\mathrm{arg}}}\right)\right] \tag{7}$$

Here, $1 - \phi$ represents the packing density of the powder bed, $k_{316\mathrm{L}}$ the thermal conductivity of bulk 316L steel, k_{arg} the thermal conductivity of surrounding argon gas and k_{rad} represents the heat transfer due to radiation between individual particles, which can be calculated as given below.

$$k_{\mathrm{rad}} = \frac{4}{3}\sigma T^3 D_{\mathrm{pwd}} \tag{8}$$

Here, σ represents the Stefan–Boltzmann constant, while D_{pwd} represents the mean diameter of the particles. The effective thermal conductivity in Eq. (7) allows modelling of the heat transfer by thermal conduction through solid granular material, thermal conduction due to argon gas, and heat transfer due to radiation. For the calculation of apparent density of the powder bed, following equation is used.

$$\rho_{\mathrm{pwd}} = \rho_{316\mathrm{L}}(1 - \phi) \tag{9}$$

where $\rho_{316\mathrm{L}}$ represents the bulk density of 316L steel and ρ_{pwd} represents the apparent density of the powder bed. The plots for the material properties are given in Figs. 1, 2 and 3.

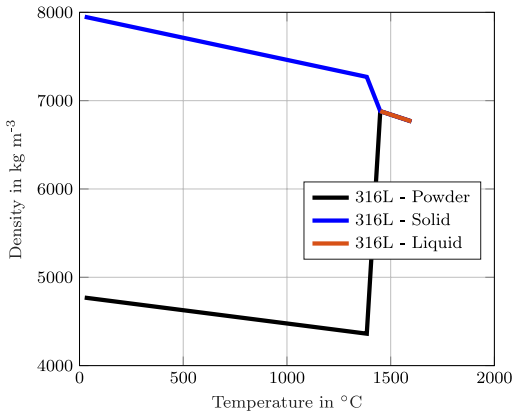

Fig. 1 Variation of density with the temperature for solid steel 316L and powder

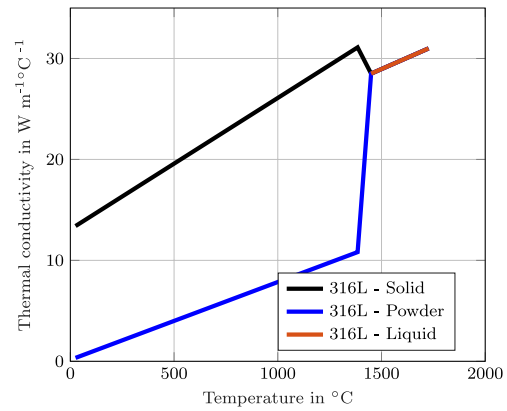

Fig. 2 Variation of thermal conductivity with the temperature for solid steel 316L and powder bed

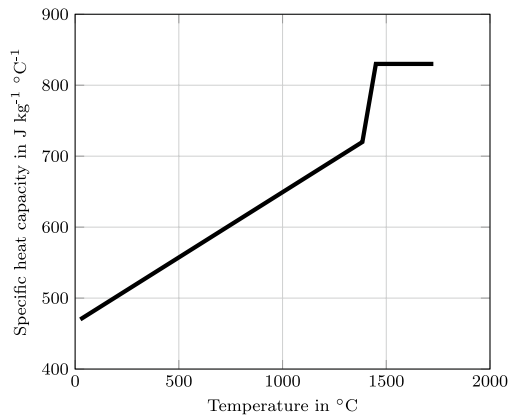

Fig. 3 Variation of specific heat capacity with the temperature for 316L

2.2 Heat source modelling

As mentioned before, the numerical modelling of the LPBF process can be carried out at different scales. This can be performed at the scale of powder (mesoscale), where the volumetric heat source tracks the laser path and can predict the thermal field and size of the melt pool. An analysis at microscale can predict the evolution of grains. Although, the aforementioned scales allows an in-depth study of the process, it comes at significant computational cost. In the current work, the residual temperature at the end of the inter-layer time of each layer is of interest. For this purpose, a macroscale model is deemed sufficient. With this simplified and computationally efficient approach, the residual temperature for each layer can be calculated. Figure 4 shows different levels of abstraction for the application of the heat source.

In the current work, the abstraction level shown on the left side in Fig. 4 is used. Instead of tracing each laser scan vector for a layer, the heat source is directly applied for the whole layer. The heat source at macro-scale Q_v is derived from the heat source at mesoscale q_v as given below.

$$\int Q_v \mathrm{d}t = \frac{1}{V} \int \int q_v \mathrm{d}v \mathrm{d}t \tag{10}$$

where V represents the volume of the layer. Using this approach, Q_v is calculated as given below.

$$Q_v = \frac{\eta P}{V} \tag{11}$$

In this equation, P represents the laser power and η represents the fraction of total energy absorbed. It is well known observation that not all of the incident energy from the laser is absorbed by the powder. A certain amount of the laser power is reflected and the rest is absorbed. Trapp et al. [20] carried out a detailed study on the absorption measurement of metal powder. They studied the effect of laser power and scanning velocity on absorptivity. Based on calorimeter measurements, the effective absorptivity for different materials, including 316 L, was measured. In the current study, an estimated value of 0.75 for η is used based on the results of Trapp et al. [20] for the deep penetration mode welding. This is chosen as the experiments used for the model validation showed melt pools with an aspect ratio greater than 4:5 (depth:width), which is a good indicator for welding in the deep penetration mode [4]. From welding literature, a critical power density of greater than 10^6 W/cm^2 is known to result in an onset of significant material evaporation and the development of a vapor capillary the so called keyhole [21].

The laser beam is reflected multiple times at the keyhole wall which leads to increased absorption of laser power. While working in this mode, several previous solidified

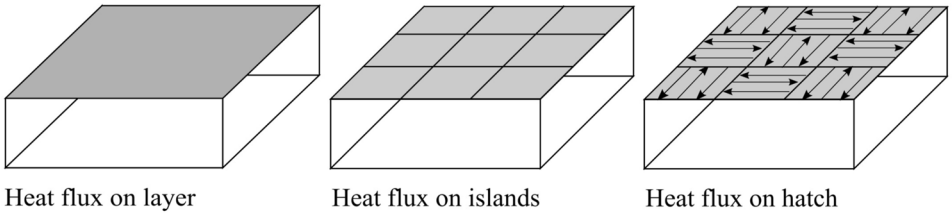

Fig. 4 Different approaches for the application of a volumetric heat source: (left) heat application on whole layer, (middle) heat application on islands, (right) heat source tracing laser path

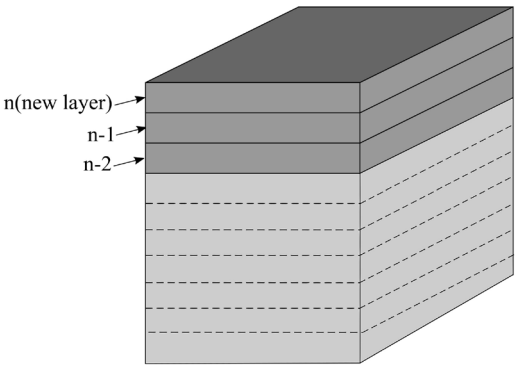

Fig. 5 Schematic diagram for application of heat source to several layers

layers in addition to the new powder layer get molten depending on the penetration depth, as shown, e.g., by Ulbricht et al. [22]. Keeping in view such an experimental observation, it is predefined for the model that the heat source acts on three successive layers for scanning of each layer. This phenomenon is illustrated in Fig. 5. For scanning of layer n, layer $n-1$ and layer $n-2$ is also subjected to heat source. Therefore, the heat source is applied to a layer more than once, which is also observed during experiments.

2.3 Geometry

In our study, a cuboidal shaped LPBF manufactured part is considered. For the construction of such a geometry, the laser scans a cross section area with a dimension of 20 mm by 13 mm along with a height of up to 114.5 mm, see Sect. 3 for details. The geometry is shown in Fig. 6. In LPBF, each layer has a region which is melted to form solid part and it is surrounded by powder which does not melt. For the modelling, the surrounding powder, which acts as a heat sink, is also considered. In Fig. 6, the region B represents the surrounding powder while region A represents the region which is to be built. The cross section of the square shaped surrounding region B, is almost twice the dimension of region A, which is 40 mm by 40 mm. In Fig. 6, region C represents the base plate, which is made from austenitic stainless steel AISI314.

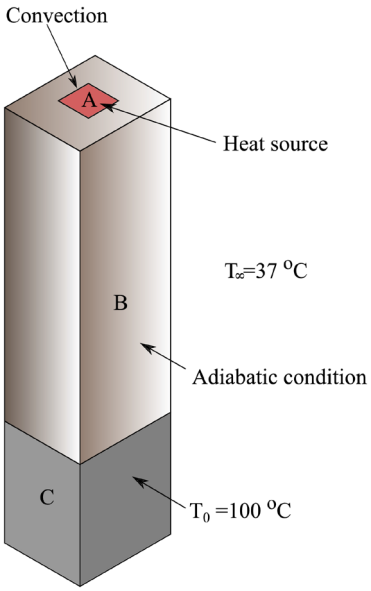

Fig. 6 Representation of the geometry to be built by the LPBF process with region A representing the build part, region B the surrounding powder and region C is the base plate

As an initial boundary condition, the temperature of region C, see Fig. 6, is taken as 100 °C for the FEM model. This corresponds to the preheating temperature of the base plate during the experiment. The region B and C is initially assumed to be at 37 °C ambient temperature. The ambient temperature within the build chamber was obtained from the internal temperature sensors of th LPBF machine. For the heat loss from the top of every newly built layer to the build chamber, a convection boundary condition is applied. While for the boundary of region B, an adiabatic boundary condition is assumed. For region A, a volumetric heat source is applied for every layer, which is explained in detail in Sect. 2.2.

3 Experiments

3.1 Material

The material used for the experiments was stainless steel 316L supplied by SLM Solutions Group AG, Lübeck,

Table 1 Powder properties according to supplier's information

Properties	Values
D_{10} in µm	18.22
D_{50} in µm	30.50
D_{90} in µm	55.87
Mean diameter in µm	34.69
Apparent density in g/cm^3	4.58

Germany. The powder properties are given in Table 1. The chemical composition of the powder is give in Table 2.

3.2 LPBF processing conditions

The manufacturing system was a commercial single laser LPBF system of type SLM280HL (SLM Solutions Group AG, Lübeck, Germany). A bi-directional scanning strategy with 90° rotation of the scan field after each layer was chosen. The scanning vectors proceeded parallel to the specimen's edges, see Fig. 7.

The processing parameters can be found in Table 3. The specimens were manufactured at three different levels of ILT, hereafter named short, intermediate, and long. The process run in argon gas atmosphere with an maximum residual oxygen level of 0.1%. The parts were manufactured on a build plate of stainless steel 314.

During the manufacturing of the specimens, thermographic measurements were conducted which are described in Sect. 3.3.

3.3 Temperature measurement

An off-axis thermographic measurement set-up was used to monitor the thermal emissions of the specimens during the manufacturing process. The camera used was a mid-wave infrared (MWIR) camera of type ImageIR8300 (InfraTec GmbH, Dresden Germany), which had optical access to the build process via a sapphire window in the ceiling of the process chamber. Its optical path was tilted by two gold coated mirrors to have a nearly perpendicular view on the build plane. Figure 8 shows a schematic of the set-up. The camera was sensitive within a spectral range from 2 to 5.7 µm and was equipped with a 25 mm objective. The resulting spatial resolution was 420 µm/pixel. The measurements were conducted at a frame rate of 600 Hz. The same monitoring set-up was used and described in detail in [4, 24].

As the MWIR camera was calibrated for black body radiation (emissivity ϵ equals 1) by its vendor, an emissivity correction of the acquired signals was necessary to get information on real temperature values, since the emissivity

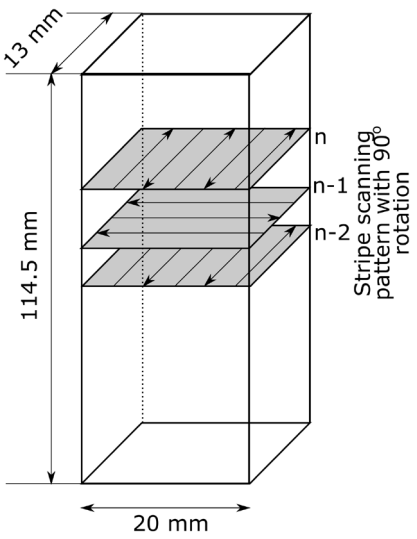

Fig. 7 Specimen geometry and schematic of scanning strategy

Table 3 Processing parameters for LPBF of 316L

Processing parameters	Level
Layer thickness	0.05 mm
Laser power	275 W
Hatch distance	0.12 mm
Preheating temperature	100 °C
Inter-layer time	Short: 18 s
	Intermediate: 65 s
	Long: 116 s
VED	Low: 49.12 J mm^{-3}
	Basis: 65.48 J mm^{-3}
	High: 81.85 J mm^{-3}

Table 2 Chemical composition of the 316L raw powder material and the respective min. and max. values as per the material specification by DIN EN 10088-3 [23]

Specification	C	Si	Mn	P	S	Cr	Mo	Ni	N	Fe
Min.	–	–	–	–	–	16.5	2.0	10.0	–	bal.
Max.	0.03	1.0	2.0	0.045	0.03	18.5	2.5	13.0	0.1	bal.
Powder	0.017	0.6	0.92	0.012	0.004	17.7	2.35	12.6	0.1	bal.

The figures express mass fractions in %

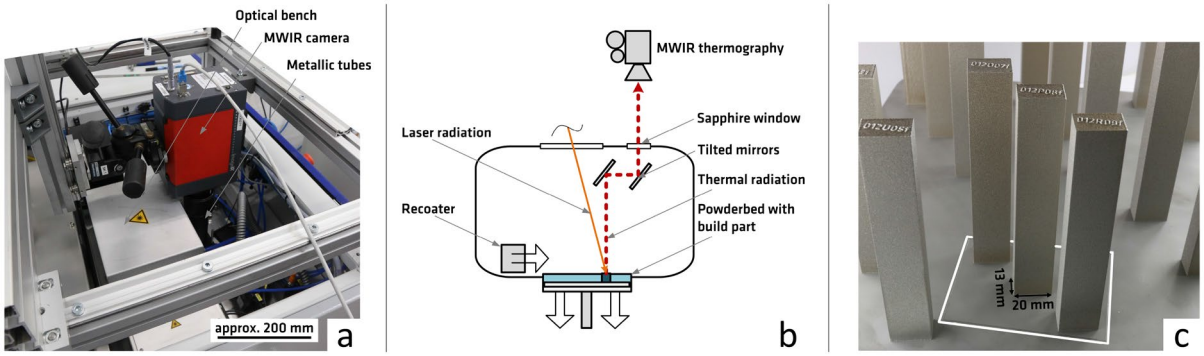

Fig. 8 MWIR camera set up and LPBF specimens: **a** photograph of a top view of the set up with the MWIR camera on top of the build chamber ceiling (Source: Mohr et al. [25]); **b** schematic of the MWIR camera set-up (Source: Mohr et al. [24]), **c** photograph of LPBF specimens produced at intermediate ILT, the white rectangle highlights the field of view of the MWIR camera on the build plate

ϵ of metallic surfaces is much smaller than 1. For this reason, extensive experiments were conducted for the determination of the emissivity of 316L LPBF surfaces as well as for the emissivity of 316L powder layers in a preliminary study [25].

The experimental temperature values of the present study represent the preheating temperature of a specimen acquired at a freshly powder recoated surface prior to the subsequent laser exposition. In the centre of each specimen an area of 11 pixels × 11 pixels was selected and the IR-signals were averaged and corrected using a conversion based on the determined apparent emissivity values. In the knowledge of the experimentally determined emissivity values for 316L powder layers at different relevant temperatures, it was possible to calculate real temperatures in °C from the obtained IR-Signal values of the MWIR camera. This procedure and the respective emissivity values per camera calibration range are described in detail in the respective studies [7, 25].

4 Results and discussion

For the validation of numerical model, the real averaged temperature at the end of the ILT of each layer, which basically is the preheating temperature for the new layer, is compared with the averaged temperature from the simulation results. For the experimental measurement of the thermal history, the chosen region and the details of thermal camera measurements are given in Sect. 3. For the simulation, the region and the chosen time scale for the measurement of the temperature is same as in experiment. For the averaging procedure, an element with a size of 6 mm by 6 mm at the centre of the built part is chosen, which nearly corresponds to the size of the observation field in the experiment. For this element, the nodal temperature is averaged with the number of nodes. The initial and boundary condition for the problem considered in the current study is described in detail in Sect. 2.

The duration of the application of the volumetric heat source per layer is calculated from the total amount of time spent by the laser for scanning whole layer. While the duration for the cooling phase, when no heat is applied, is calculated from the ILT. For the build part, hexahedral elements with linear shape functions are used. The model contains 112,680 elements and 146,736 nodes. For the simulation of the layerwise exposition of material, element birth and death technique as described in Ansys® [17] is used.

Figure 9 shows the temperature field at the end of the ILT, which is obtained from the solution of the numerical model. The gradual heat accumulation along the height until 70 mm can be seen in Fig. 9 (left). Considering the top surface at 70 mm, the central solidified region, which is exposed to the laser (represented as region A in Fig. 6), has nearly uniform temperature, while the region in the vicinity, which corresponds to the surrounding powder (represented as region B in Fig. 6) is at relatively lower temperature, see Fig. 9 (right). The heat dissipation to the surrounding powder is often modelled by application of convection boundary condition on the boundary of solidified part. For instance, Denlinger et al. [26] modelled the heat loss from the built part to the surrounding powder by application of convection boundary condition. The convection coefficient was determined by correlation of thermal results with the experimentally determined temperature measurements. Li et al. [15] also used similar approach for prediction of residual stresses and part distortion during SLM process. In this work, however, the surrounding powder is explicitly modelled and absorbs the heat from the exposed region via conduction.

Figure 10 shows the accumulation of heat over the height of the built part. The x-axis represents the layer number while the y-axis represents the temperature at the end of inter-layer time. Since the base plate is preheated to 100 °C, the initial temperature of layers is close to 100 °C. Up to

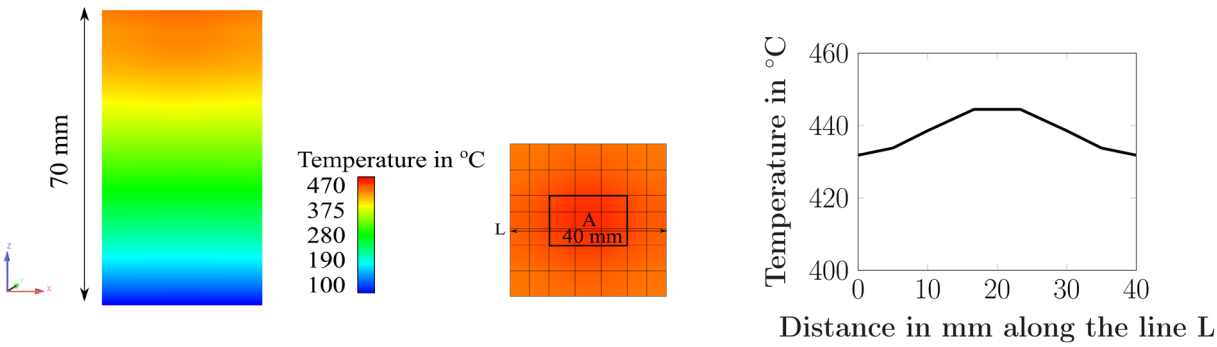

Fig. 9 Representation of thermal field from simulation shown at 70 mm of build height at the end of ILT for short ILT, scanning velocity 700 mm/s and power 275 W. Side view (left), top view (middle) and nodal temperature along line L (right)

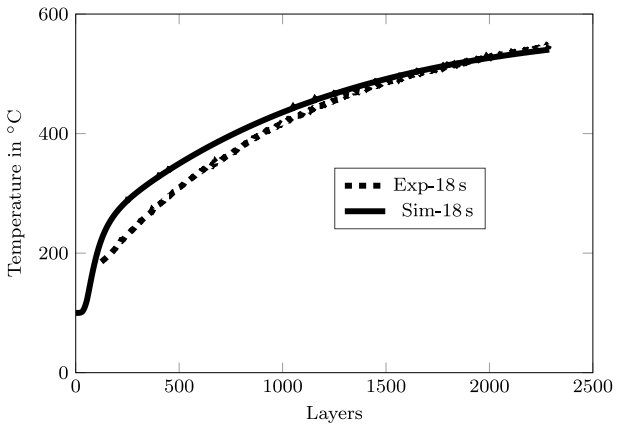

Fig. 10 Comparison of simulation and experimental results for short inter-layer time 18 s, a constant scanning velocity of 700 mm/s and a constant power of 275 W

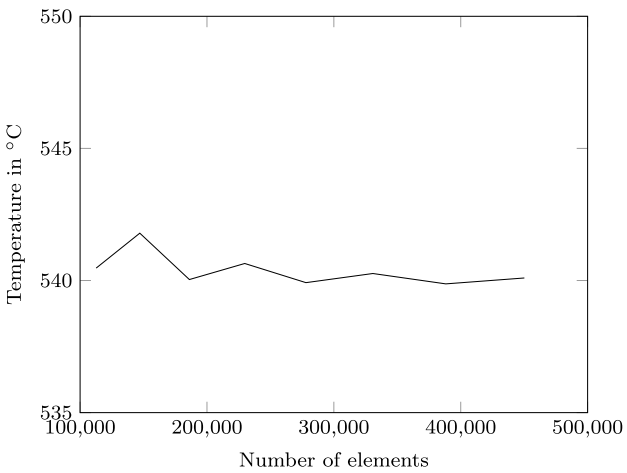

Fig. 11 Mesh sensitivity analysis

layer 180, the gradient of the curve remained nearly constant and reached temperature of up to 230 °C. After layer 180, the gradient of curve decreased. With the increase in temperature difference from the ambient temperature, the gradual decrease in gradient can be attributed to the combined effect of increased heat loss due to convection to the surrounding and heat dissipation to the powder in region B. For the heat loss via convection to the build chamber, a convection parameter, via calibration, 0.1 W/m^2 is chosen. From Fig. 10, it can be seen that in the beginning the temperature of the simulation results is higher than the experimental observations while for later layers, they are in good agreement with each other. Overall, the simulation model can predict the experimentally observed heat accumulation to a sufficient accuracy.

To study the effect of the mesh size on the resultant solution, a mesh sensitivity analysis is carried out, which can be seen in Fig. 11. The *y*-axis of Fig. 11 shows the peak temperature reached at the end of the ILT for the very last layer of the build part. The *x*-axis represents the number of elements, where the mesh is refined for each layer to study its effects on convergence of the solution. It can be seen from Fig. 11 that the initially chosen mesh density, 112,680 elements, is sufficient for a converged solution.

Mohr et al. [4, 7] studied the effect of different combinations of VED and ILT on LPBF based manufactured specimens. The geometry, combinations of VEDs and ILTs used in their work is shown in Fig. 7 and listed in Table 3, respectively. It was observed that the VED and ILT has a profound effect on grain size, melt pool size and on the presence of porosity for LPBF based built parts. For short ILT, the mean low angle grain boundary sub-grain size increased from 458 μm^2 for low VED to 1386 μm^2 for high VED for the top region [7]. For a fixed value of VED, the size increased with the decrease in ILT. A similar trend was also observed for the melt pool depth which increased with the increase in VED. For short ILT, the melt pool depth was 388 µm for high VED while it was 207 µm for low VED [4]. With regard to porosity, it became significant for high VED and short ILT. The reader is referred to the work of Mohr et al.

[4, 7] for the complete details regarding different combinations and their effect on grain size and melt pool size. From their work, it can be inferred that the heat accumulation is of particular interest for a homogeneous properties throughout a part manufactured via LPBF. With the accumulation of heat, defects like porosity and undesired microstructure might appear. In the next sections, the simulation results are compared with experimental results when different ILTs and different VEDs are applied.

4.1 Different ILT

In this section, a comparison of simulations and experiments for different ILTs is performed. As also defined by Mohr et al. [4], short (18 s), medium (65 s), and long ILT (116 s) is used. In Fig. 12, experimental and simulation results are compared for different ILTs.

In all these cases, power (275 W), scanning velocity (700 mm/s), and layer thickness (50 µm), which among others determines the volumetric energy density, is kept constant. From Fig. 12, it can be seen that the experimental data below a threshold temperature is missing. In Sect. 3, it was mentioned that the infrared camera can be used to obtain thermographic measurements within particular calibration ranges. Outside of the respective upper or lower temperature thresholds of these calibration ranges, the obtained data are not valid and are, therefore, not displayed in the figure.

The effect of the ILT on heat accumulation can be seen in Fig. 12. In case of short ILT, the maximum temperature reached in the experiments is 545 °C while for medium ILT, the maximum temperature reached is 230 °C. In case of long ILT, the duration for dissipation of heat is sufficient. Resultantly, there is no significant accumulation of heat. The maximum temperature reached in this case is 170 °C.

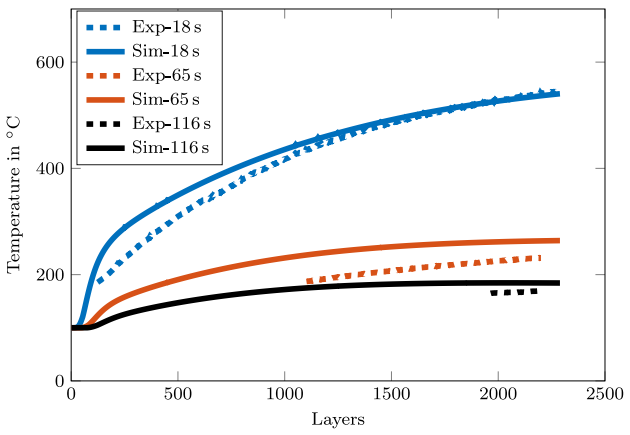

Fig. 12 Comparison of simulation and experimental results for different inter-layer times, at a constant scanning velocity of 700 mm/s and a constant laser power of 275 W

For short ILT, initially, there is a steep increase in temperature and for later layers, the gradient of the curve decreased, which was also described in the previous section. Whereas for medium ILT, the increase in temperature during the build-up of the first few layers is relatively less. Unlike short ILT, for medium ILT, the duration allows for more heat dissipation before the next energy input. In case of long ILT, the increase in temperature remained lowest and for later layers, the curve was nearly flat, indicating that an equilibrium state between energy intake and energy dissipation is reached. The difference in peak temperature between short and medium ILT condition is relatively higher as compared to the difference between medium and long ILT condition.

This trend is followed by the simulation results. There is a good agreement between the simulation and experimental results for the short ILT. The difference in the peak temperatures for both cases is 7 °C. As in the experiments, the rate of temperature increase or the gradient of the curve was higher in the beginning and then decreased for later layers. In case of medium and long ILT, the peak temperature at the end of build was higher for simulation results as compared to the experiments. The difference between experimental and simulation results is nearly 30 °C for medium ILT while for long ILT, it is 14 °C. In simulation, the peak temperature are 263 °C for medium ILT and 184 °C for long ILT. It should be remarked that not all physical effects observed during LPBF based manufacturing can be reproduced by macroscale simulation. For instance, Mohr et al. [4] reported deviations in meltpool sizes in dependence of ILT and built height. As also described by Ye et al. [27], an increase in melt pool depth can be related to a possible increase of energy absorption and vice versa. In the current model, the absorptivity coefficient, which is adjusted for the short ILT condition, might deviate for medium and long ILT. Resultantly, the usage of such an absorption coefficient, which is too high, might have overestimated the simulation results.

In addition, it should be remarked that the experimental data shown in the current paper is based on mean values of experimental observations and a certain degree of uncertainty in measurements exists, which is described in detail by Mohr et al. [7, 25]. Therefore, it can be concluded that the simulation results are still within a good agreeable range of experiments.

4.2 Different VED

In addition to the ILT, the scanning velocity v is also varied to obtain different values of VEDs. The effect of this variation on resultant heat accumulation is also studied. The scanning velocities used are 933 mm/s, 700 mm/s and 560 mm/s, which results in VED having values of 49.12 J/mm^3 (low), 65.48 J/mm^3 (basis) and 81.85 J/mm^3 (high), see Table 3.

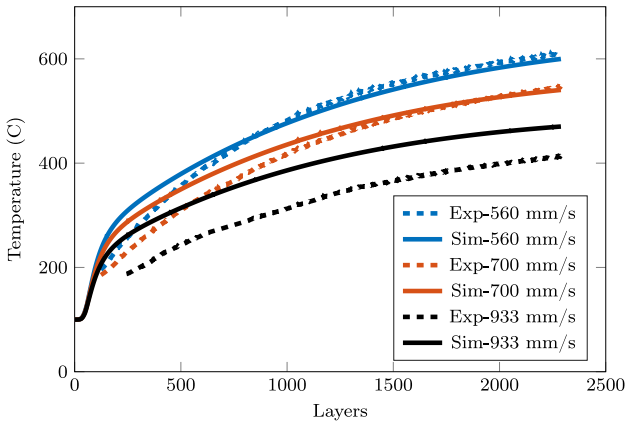

Fig. 13 Comparison of simulation and experimental results for different velocities, short inter-layer time 18 s and a constant power of 275 W

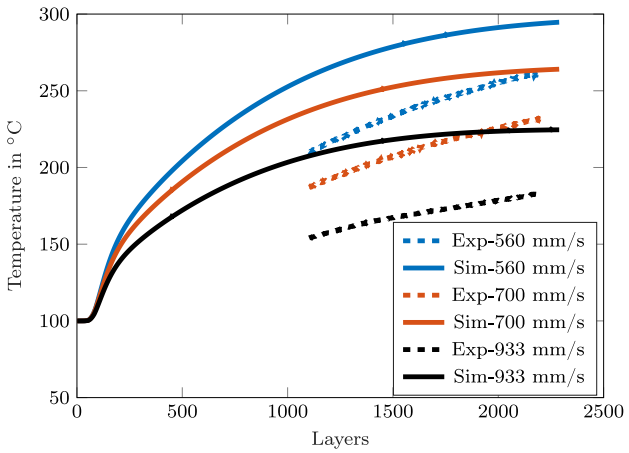

Fig. 14 Comparison of simulation and experimental results for different velocities, medium inter-layer time 65 s and a constant power 275 W

For the parametric study, the ILT is fixed and VED is varied. This is repeated for all three combination of ILTs.

Figure 13 shows the variation in accumulation of heat for different values of VEDs for short ILT (18 s). The experimental results clearly show that the higher value of VED (which corresponds to lower values of scanning velocity) results in higher value of peak temperature. Therefore, with the increase in VED, an increase in heat accumulation is observed. However, in all cases, the general shape of the curve remains the same. The simulation results were in good agreement with the experimental results. The general trend was also well captured by the FEM simulation. However, the peak temperature predicted by the simulation was slightly lower than the experiments for high VED. For low VED, the peak temperature predicted by the simulation was higher than the experiment and the difference between the results from the simulation and from the experiments are relatively higher. Again, the usage of a constant absorption coefficient in the simulation regardless of the VED is likely to be the source of these deviations. As shown by Mohr et al. [4], the melt pool depth varied significantly with varying VED. It showed values of about 350 µm for high VED, 259 µm for basis VED and 188 µm for low VED in the lower part of specimens built with short ILT where the differences in the preheating temperature were still comparably small. According to Trapp et al. [20], there is a significant change of the absorption coefficient in the transition region from conduction or transition mode welding to keyhole mode welding. They presented experimentally determined values for the absorption coefficient between around 0.4 and 0.78, from which the latter value is the saturation value which is applicable when deep keyhole melt pools are developed. This leads to the assumption, that the melt pools developed at low VED could rather be associated to the lower absorption values and the early onset of the keyhole regime. This displays a sensitivity of the model to processing parameter dependant absorption coefficients. The model calibrated for standard VED (700 mm/s), shows the most deviation corresponding to the velocity of 933 mm/s. For the material and processing parameters in the current study, the functional relationship between the scanning velocity and absorption coefficient is not known. In work of Trapp et al. [20], it was already shown that such a relation is not linear. For higher velocities, the deviation of absorption coefficient might be higher in comparison to the lower velocities (Fig. 14).

For the analysis with medium ILT, the general behaviour was similar to the short ILT, where a decrease in heat accumulation with the decrease in VED is observed. There was again a general good agreement between simulation and experimental results. On average, the difference between simulation and experimental results was 30 °C. In contrast to short ILT, the gradient of the curve was relatively less for layers within 500–2290 range. For experiments, the data below a threshold temperature value is missing in Fig. 15. This is due to thermographic measurement ranges used in the experiment. In previous sections, an explanation regarding the deviation in results was already given. As explained earlier, the change in absorption coefficient due to combined effect of ILT and scanning velocity might be responsible for the deviations. A detailed study in this regard can be part of future research.

Finally, in Fig. 15, a comparison for long ILT is performed. In this case, the average difference between the experimental and simulation results is 15 °C. The reasons for deviation between simulation and experimental results were also explained in previous sections. It can be seen from the figure, that the curve nearly remained flat for later layers. The ILT was sufficient to dissipate the heat and to avoid its accumulation for later layers of the built part. In case of

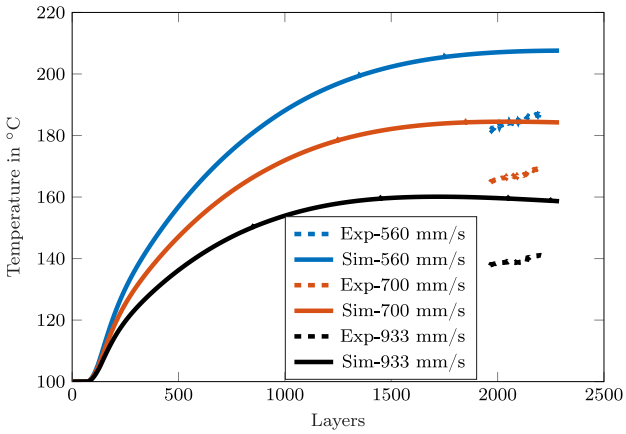

Fig. 15 Comparison of simulation and experimental results for different velocities, long inter-layer time 116 s and a constant power of 275 W

long ILT, the thermal equilibrium for simulation seems to be achieved earlier than in the experiments. In the experiments, there is still a monotonic increase in temperature observed. In addition, heat dissipation via convection could be studied in more detail. In Lu et al. [28], a temperature dependant convection coefficient was used, where an increase in the coefficient's value with the increase in temperature was considered. A similar study can also be part of further investigation for the current model, which might reveal the deviation in the trends of simulation from the experiments.

Although, the accuracy with which the presented numerical model can predict the experimentally observed heat accumulation is sufficient to identify the regions of severe heat accumulation, there are certain limitations of the presented model. The model does not include processing parameter dependant deviations of the absorption coefficient. For the scanning velocities and VED considered in this paper, further experiments can assist to determine the coefficient's value. Furthermore, additional experiments could also reveal if there is a variation in its value over the build height due to changing preheating temperatures. This can later be included in the numerical model as an analytical function. Ulbricht et al. [29] reported that two different scanning strategies resulted in different heat accumulations. For the presented macroscale model, this effect cannot be reproduced, as the scanning strategy itself is not included. In addition, the thermal gradient observed during heating and cooling of a part in the experiment is difficult to be reproduced in a macroscale model. Overall, the model provides a computationally efficient approach, which can be used for prediction of heat accumulation for LPBF based built part with a reasonable accuracy. For an optimization study in the future, the computational speed of the experimentally validated model allows several numerical evaluations. The optimization can be performed in terms of design to find suitable geometry or a set of processing parameters that will reduce the accumulation of heat.

5 Conclusion

In this work, a macroscale FEM model was used to determine the accumulation of heat during LPBF manufacturing under a combination of different processing conditions. The simulation results were compared with experimental measured temperature data. Experimental results, presented by Mohr et al. [7], together with the FEM based simulation model revealed that ILT and VED are some of the important parameters responsible for heat accumulation. From the comparative study of the model, the following conclusions can be drawn:

- A decrease in ILT leads to an increase in heat accumulation. The peak temperature for short ILT was almost three times more than for long ILT.
- Heat accumulation becomes more pronounced with the increase in build height for short ILT. For long and medium ILT, the heat accumulation with the increase in build height was less as compared to short ILT.
- For a constant ILT, an increase in VED leads to an increase in peak temperature and heat accumulation.
- The easy to use macroscale model is feasible to simulate the accumulation of heat in good agreement to experimental data. Among other factors, the deviation of experimental and simulation results possibly can be attributed to the absorption coefficient. The usage of a laser velocity dependant coefficient can possibly improve the simulation results.

Overall, the numerical model was able to predict the experimental results with sufficient accuracy. With the validation of the numerical model, it can be used for further investigations for different geometries, which will allow design optimization. Furthermore, it can be used for the determination of an optimum combination of processing parameters. The computational speed up obtained using such a simplified model can be used for several evaluations for determination of the processing parameters that will reduce the heat accumulation.

The study carried out in this paper also provides a good basis for a detailed mesoscale analysis of LPBF based parts in the future. This will require a combined meso-macro scale analysis. For a detailed mesoscale analysis at a certain layer, the temperature field of already solidified preceding layers can be obtained from a macroscale analysis. The solution from macroscale, which will act as preheating temperature, will be used as an initial condition for the mesoscale analysis. Such a strategy can be used for a computationally

efficient and detailed analysis at any layer of LPBF based manufactured part.

Acknowledgements This research was funded by BAM within the focus area Materials.

Author contributions MC: conceptualization, investigation, formal analysis, validation, writing—original draft. GM: methodology, validation, data curation, writing—review and editing. KH: conceptualization, writing—review and editing, supervision.

Funding Open Access funding enabled and organized by Projekt DEAL.

Declarations

Conflict of interest The authors have no conflicts of interest to declare.

References

1. Liverani E, Toschi S, Ceschini L, Fortunato A (2017) Effect of selective laser melting (SLM) process parameters on microstructure and mechanical properties of 316l austenitic stainless steel. J Mater Process Technol 249:255–263
2. Sames WJ, List F, Pannala S, Dehoff RR, Babu SS (2016) The metallurgy and processing science of metal additive manufacturing. Int Mater Rev 61(5):315–360
3. Bertoli US, Wolfer AJ, Matthews MJ, Delplanque J-PR, Schoenung JM (2017) On the limitations of volumetric energy density as a design parameter for selective laser melting. Mater Des 113:331–340
4. Mohr G, Altenburg SJ, Hilgenberg K (2020) Effects of inter layer time and build height on resulting properties of 316L stainless steel processed by laser powder bed fusion. Addit Manuf 32:101080
5. Denlinger ER, Heigel JC, Michaleris P, Palmer T (2015) Effect of inter-layer dwell time on distortion and residual stress in additive manufacturing of titanium and nickel alloys. J Mater Process Technol 215:123–131
6. Costa L, Vilar R, Reti T, Deus A (2005) Rapid tooling by laser powder deposition: process simulation using finite element analysis. Acta Mater 53(14):3987–3999
7. Mohr G, Sommer K, Knobloch T, Altenburg SJ, Recknagel S, Bettge D, Hilgenberg K (2021) Process induced preheating in laser powder bed fusion monitored by thermography and its influence on the microstructure of 316L stainless steel parts. Metals 11(7):1063
8. Williams RJ, Piglione A, Rønneberg T, Jones C, Pham M-S, Davies CM, Hooper PA (2019) In situ thermography for laser powder bed fusion: effects of layer temperature on porosity, microstructure and mechanical properties. Addit Manuf 30:100880
9. Khairallah SA, Anderson AT, Rubenchik A, King WE (2016) Laser powder-bed fusion additive manufacturing: physics of complex melt flow and formation mechanisms of pores, spatter, and denudation zones. Acta Mater 108:36–45
10. Denlinger ER, Jagdale V, Srinivasan G, El-Wardany T, Michaleris P (2016) Thermal modeling of Inconel 718 processed with powder bed fusion and experimental validation using in situ measurements. Addit Manuf 11:7–15
11. Khan K, Mohr G, Hilgenberg K, De A (2020) Probing a novel heat source model and adaptive remeshing technique to simulate laser powder bed fusion with experimental validation. Comput Mater Sci 181:109752
12. Fürstenau J-P, Wessels H, Weißenfels C, Wriggers P (2020) Generating virtual process maps of SLM using powder-scale SPH simulations. Comput Particle Mech 7(4):655–677
13. Russell M, Souto-Iglesias A, Zohdi T (2018) Numerical simulation of laser fusion additive manufacturing processes using the SPH method. Comput Methods Appl Mech Eng 341:163–187
14. Afrasiabi M, Lüthi C, Bambach M, Wegener K (2021) Multi-resolution SPH simulation of a laser powder bed fusion additive manufacturing process. Appl Sci 11(7):2962
15. Li C, Liu J, Fang X, Guo Y (2017) Efficient predictive model of part distortion and residual stress in selective laser melting. Addit Manuf 17:157–168
16. Denlinger ER, Irwin J, Michaleris P (2014) Thermomechanical modeling of additive manufacturing large parts. J Manuf Sci Eng 136:6
17. Ansys® Academic Research Mechanical, Release 2019R3
18. Mills KC (2002) Recommended values of thermophysical properties for selected commercial alloys. Woodhead Publishing, Sawston
19. Sih SS, Barlow JW (2004) The prediction of the emissivity and thermal conductivity of powder beds. Part Sci Technol 22(4):427–440
20. Trapp J, Rubenchik AM, Guss G, Matthews MJ (2017) In situ absorptivity measurements of metallic powders during laser powder-bed fusion additive manufacturing. Appl Mater Today 9:341–349
21. Dilthey U (2006) Schweißtechnische Fertigungsverfahren 1: Schweiß-und Schneidtechnologien. Springer, Berlin
22. Ulbricht A, Mohr G, Altenburg SJ, Oster S, Maierhofer C, Bruno G (2021) Can potential defects in LPBF be healed from the laser exposure of subsequent layers? A quantitative study. Metals 11(7):1012
23. Briefs Günter (2014) Nichtrostende Stähle-Teil 3: Technische Lieferbedingungen für Halbzeug, Stäbe, Walzdraht, Gezogenen Draht, Profile und Blankstahlerzeugnisse aus korrosionsbeständigen Stählen für allgemeine Verwendung. DIN, Berlin
24. Mohr G, Scheuschner N, Hilgenberg K (2020) In situ heat accumulation by geometrical features obstructing heat flux and by reduced inter layer times in laser powder bed fusion of AISI 316L stainless steel. Proced CIRP 94:155–160
25. Mohr G, Nowakowski S, Altenburg SJ, Maierhofer C, Hilgenberg K (2020) Experimental determination of the emissivity of powder layers and bulk material in laser powder bed fusion using infrared thermography and thermocouples. Metals 10(11):1546
26. Denlinger ER, Gouge M, Irwin J, Michaleris P (2017) Thermomechanical model development and in situ experimental validation of the laser powder-bed fusion process. Addit Manuf 16:73–80
27. Ye J, Khairallah SA, Rubenchik AM, Crumb MF, Guss G, Belak J, Matthews MJ (2019) Energy coupling mechanisms and scaling behavior associated with laser powder bed fusion additive manufacturing. Adv Eng Mater 21(7):1900185

28. Lu X, Lin X, Chiumenti M, Cervera M, Li J, Ma L, Wei L, Hu Y, Huang W (2018) Finite element analysis and experimental validation of the thermomechanical behavior in laser solid forming of Ti-6Al-4V. Addit Manuf 21:30–40
29. Ulbricht A, Altenburg SJ, Sprengel M, Sommer K, Mohr G, Fritsch T, Mishurova T, Serrano-Munoz I, Evans A, Hofmann M et al (2020) Separation of the formation mechanisms of residual stresses in lpbf 316l. Metals 10(9):1234